JACS
JOURNAL OF THE AMERICAN CHEMICAL SOCIETY
Article
pubs.acs.org/JACS

Mono-, Few-, and Multiple Layers of Copper Antimony Sulfide ($CuSbS_2$): A Ternary Layered Sulfide

Karthik Ramasamy,*[,†,§] Hunter Sims,[‡,§,∥] William H. Butler,[‡,§] and Arunava Gupta*[,†,§]

[†]Department of Chemistry, [‡]Department of Physics, and [§]Center for Materials for Information Technology, The University of Alabama, Tuscaloosa, Alabama AL-35487, United States

Supporting Information

ABSTRACT: Layered materials with controlled thickness down to monolayer are being intensively investigated for unraveling and harnessing their dimension-dependent properties. Copper antimony sulfide ($CuSbS_2$) is a ternary layered semiconductor material that has been considered as an absorber material in thin film solar cells due to its optimal band gap (~1.5 eV) with high absorption coefficient of over $>10^4$ cm^{-1}. We have for the first time developed solution-based approaches for the synthesis of mono-, few-, and multiple layers of $CuSbS_2$. These include a colloidal bottom-up approach for the synthesis of $CuSbS_2$ nanoplates with thicknesses from six layers to several layers, and a hybrid bottom-up-top-down approach for the formation of $CuSbS_2$ mesobelts. The latter can be exfoliated by Li-ion intercalation and sonication to obtain layers down to monolayer thickness. Time-dependent TEM studies provide important insights into the growth mechanism of mesobelts. At the initial stage the nanoplates grow laterally to form nanosheets as the primary structure, followed by their folding and attachment through homoepitaxy to form prolate-like secondary structures. Eventually, these prolate-like structures form mesocrystals by oriented attachment crystal growth. The changes in optical properties with layer thickness down to monolayers have been studied. In order to understand the thickness-dependent optical and electrical properties, we have calculated the electronic structures of mono- and multiple layers (bulk) of $CuSbS_2$ using the hybrid functional method (HSE 06). We find that the monolayers exhibit noticeably different properties from the multilayered or the bulk system, with a markedly increased band gap that is, however, compromised by the presence of localized surface states. These localized states are predominantly composed of energetically favorable Sb p_z states, which break off from the rest of the Sb p states that would otherwise be at the top of the gap. The developed solution-based synthesis approaches are versatile and can likely be extended to other complex layered sulfides.

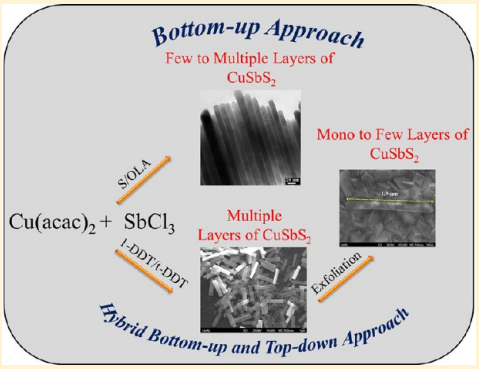

INTRODUCTION

Layered materials have been enjoying a resurgence of interest in recent years because of their dimension-dependent properties, primarily fueled by the astonishing success of graphene.[1−3] Many layered materials have recently been explored with the aim of unraveling their thickness-dependent properties.[4,5] The large family of layered materials includes carbon group elements, transition-metal chalcogenides, oxides, oxychlorides, silicates, nitrides, Zintl phases, etc.[6] Among these, the transition-metal dichalcogenides (TMDCs) are the most intensively studied class of materials next to graphene because of their wide potential applicability in microelectronics, spin and valley-tronics, thermoelectrics, catalysis, batteries, lubricants, etc.[7,8] In particular, molybdenum and tungsten dichalcogenides, referred to as inorganic fullerenes, exhibit thickness-dependent indirect to direct band gap transition, resulting in an astonishing 10^4-fold enhancement in the photoluminescence.[9,10] Despite numerous investigations of different binary layered chalcogenides, studies of ternary chalcogenides have thus far not been attempted. Ternary layered chalcogenides are potentially advantageous over the binary ones since, in addition to thickness-dependent quantum confinement effects, they can provide additional degrees of freedom for tuning the electrical and optical properties. For example, the flexibility to substitute metal and chalcogenide ions in monolayer-level ternary chalcogenides can open up new avenues for future research. Thus it is important to investigate the properties of these materials at the monolayer level that may be complementary to graphene or the TMDCs.

Toward this goal, we have chosen to study copper antimony sulfide ($CuSbS_2$), which is a ternary layered semiconductor with a direct (experimental) band gap between 1.38 and 1.52 eV.[11,12] $CuSbS_2$ crystallizes in an orthorhombic crystal system with *Pnma* space group.[13] The crystal structure is composed of SbS_2 chains along the *b*-axis, which are formed by linkage of Sb square pyramids and CuS_3 chains parallel to *b*-axis, created by CuS_4 tetrahedral links. These two infinite chains are interconnected to produce sheets that are perpendicular to the *c*-axis.[14] The material can also be considered as a derivative

Received: November 18, 2013
Published: January 8, 2014

   dx.doi.org/10.1021/ja411748g | J. Am. Chem. Soc. 2014, 136, 1587−1598

of SnS, formed by replacing the Sn(IV) ions with Cu(I) and Sb(III) to produce $CuSbS_2$ (CAS).[15] CAS has thus far largely been studied as an absorber material in thin film solar cells due to its optimal band gap and high absorption coefficient of $>10^4$ cm^{-1}.[16,11] In recent years, there have been a few reports on the synthesis of $CuSbS_2$ micro and nanocrystals by hydrothermal, solvothermal, and colloidal methods.[12,13,17] However, the synthesis of mono- or few layers of $CuSbS_2$ has thus far not been reported. Herein, we report synthesis methods for obtaining mono- and few layers of $CuSbS_2$ in the form of nanoplates and mesobelts by colloidal bottom-up and hybrid bottom-up-top-down approaches, along with detailed mechanistic studies of formation. We have studied the changes in optical properties with layer thickness down to monolayers. Moreover, we have performed band structure calculations for better understanding of the thickness-dependent optical and electrical properties.

METHODS (EXPERIMENT)

All chemicals were used as received, and the solvents were dried in molecular sieves and purged with high-purity argon for 30 min before use. 1-dodecanethiol (1-DDT, 98.0%), *t*-dodecanethiol (*t*-DDT, 98.0%), and antimony chloride ($SbCl_3 \cdot 6H_2O$, 99.5%) were received from Alfa Aesar; copper acetylacetonate ($Cu(acac)_2$, ≥99.0%), and oleylamine (OLA, ≥80−90.0%) were obtained from Acros Organics and Pfaltz and Bauer. Analytical grade hexane and ethanol were obtained from Aldrich Chemical Co.

METHODS (THEORY)

All calculations were performed using the Vienna ab initio Simulation Package (VASP).[18−20] The calculations using density functional theory (DFT) were performed within the generalized gradient approximation of Perdew, Burke, and Ernzerhof (PBE).[21,22] We also employed the screened hybrid functional method of Heyd, Scuseria, and Ernzerhof (HSE06 parameters) as a compromise between accuracy and computational efficiency.[23,24] We used the projected augmented wave (PAW) pseudopotentials of Kresse and Joubert.[25,26] PBE and HSE06 calculations were performed on a 6 × 9 × 3 Γ-centered **k** mesh for the bulk structure (with a reduced mesh for the exact exchange integrals), and a 6 × 9 × 1 mesh was employed for the PBE monolayer. A smaller 3 × 5 × 1 mesh was used for the HSE06 monolayer calculations. Absorption curves were computed within HSE06 from the complex dielectric constant, which is computed via a sum over empty states (for the imaginary part) and a Kramers−Kronig relation (for the real part). The band plots were created from a Wannier basis including all Cu d, Sb s and p, and S s and p states using the WANNIER90 package.[27]

Synthesis of $CuSbS_2$ Nanoplates Layers. All experiments were carried out in a fume hood under N_2 atmosphere using a standard Schlenk line. In a typical synthesis of $CuSbS_2$, 0.5 mmol of $Cu(acac)_2$, 0.50 mmol of $SbCl_3 \cdot 6H_2O$, and 10 mL of OLA were degassed at room temperature for 15 min and then backfilled with nitrogen for 15 min. The mixture was subsequently heated to reaction temperatures between 170 and 280 °C under N_2 atmosphere. In a separate vessel, elemental sulfur (1.3 mmol) was mixed with 1 mL of OLA and degassed three times. The solution was quickly injected into the metal source mixture held at the targeted synthesis temperature, with continued stirring of the resulting mix for 10−30 min. After cooling down to room temperature, a mixture of hexane (15 mL) and ethanol (15 mL) was added to precipitate the product. The black precipitate was then isolated via centrifugation (4000 rpm/5 min). The washing process was repeated three times to ensure removal of the excess capping agent. Samples were analyzed using powder XRD, SEM, EDX, and TEM analysis.

Synthesis of $CuSbS_2$ Mesobelts Layers. The above-mentioned experimental procedure was also followed for the synthesis of mesobelts of $CuSbS_2$ but using a mixture of 1-DDT and *t*-DDT instead of sulfur in OLA.

Exfoliation of $CuSbS_2$ Layers from Mesobelts. To obtain mono- or few layers of $CuSbS_2$, we carried out a Li intercalation and exfoliation process. For this purpose, 20 mg of $CuSbS_2$ was stirred in 2 mL of butyllithium (*n*-BuLi) for 20 h. After intercalation, the mixture was centrifuged and redispersed in 10 mL of water and sonicated (100 W power) in a bath for 1 h.

Measurements. Transmission electron microscopy (TEM) analysis was performed using a FEI-Tecnai, 200 kV transmission electron microscope equipped with a CCD camera for STEM, HAADF detector, and EDX. TEM image nonlinear processing was carried out using Gatan digital micrograph version 3.4. Powder XRD patterns were recorded on a Bruker D8 instrument equipped with Cu Kα radiation source operated as a rotating anode at 40 kV and 20 mA. Scanning electron microscope (SEM) analysis was carried out using a JEOL 7000 FE SEM equipped with energy dispersive X-ray spectroscopy (EDX), wavelength dispersive X-ray spectroscopy (WDS), electron backscatter diffraction (EBSD), secondary electron (SE), backscattered electron (BE), and transmission electron (TE) detectors. Optical measurements were carried out using a Varian-Cary single beam spectrometer.

RESULTS AND DISCUSSIONS

Mono- and few layers of $CuSbS_2$ were obtained by two different methods, namely colloidal bottom-up and hybrid bottom-up-top-down approaches. In both approaches, conventional colloidal synthesis was followed to obtain $CuSbS_2$ in the form of nanoplates and mesobelts. For the synthesis of a few layers of $CuSbS_2$ in the form of nanoplates, $Cu(acac)_2$ and $SbCl_3$ were degassed in 10 mL of OLA, and the reaction vessel was then heated to 170 °C. To the heated mixture, 1 mL of sulfur dispersed in OLA was injected, and the resulting reaction mixture was maintained at 170 °C for 10 min, which yielded nearly uniform nanoplates with thickness of 6 ± 2 layers and lateral dimensions of about 450 nm. The same reaction when carried out at higher reaction temperatures and longer reaction times produced thicker plates, while essentially retaining the lateral dimensions. However, attempts to obtain fewer than six layer thick plates by decreasing the reaction time or temperature mainly produced copper sulfide (Cu_2S) and elemental antimony impurity phases. In an alternate approach to obtain mono- or few layers of $CuSbS_2$, we carried out a similar hot-injection process but used a mixture of 1-DDT and *t*-DDT as sulfur sources. This procedure produced belt-like structures with thickness of about 340 nm and length in the range of 9−10 μm. To reduce the layer thickness, these belt-like structures were stirred with *n*-BuLi at room temperature for 20 h to intercalate lithium ions between the van der Waals gaps of $CuSbS_2$ and then were sonicated. This yielded mono- or few layers of $CuSbS_2$ by exfoliation. We refer to this approach as 'hybrid bottom-up-top-down approach'. The use of other sulfonating agents, such as trioctylphosphine sulfide (TOP-S) or carbon disulfide, did not yield the desired product. A schematic representation of the methods used to produce mono- and few layers of $CuSbS_2$ is shown in schemes 1 and 2 (Figure 1).

The phase purity and crystallinity of $CuSbS_2$ obtained using the two approaches have been confirmed using powder X-ray diffraction. The diffraction measurements show that the synthesized nanoplates and mesobelts have an orthorhombic structure, without any secondary impurities. The representative XRD pattern of $CuSbS_2$ nanoplates synthesized at 280 °C is given in Figure 2a (the XRD patterns for the samples obtained at lower temperatures are shown in Figure S1). The major

dx.doi.org/10.1021/ja411748g | J. Am. Chem. Soc. 2014, 136, 1587−1598

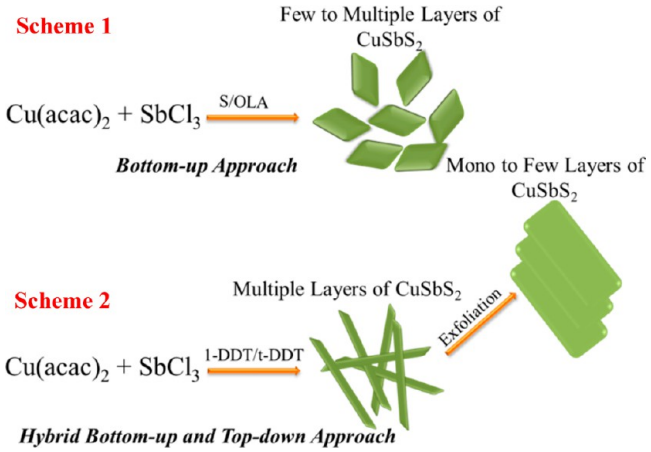

Figure 1. Schematic representation of synthesis methods used to obtain mono-, few-, and multiple layers of $CuSbS_2$.

diffraction peaks are indexed as (111), (410), (020), (301), (501), (321), (521), (131), and (212) planes of orthorhombic $CuSbS_2$ with *Pmna* space group (ICDD: 044-1417). From the diffraction pattern the lattice parameters for the $CuSbS_2$ nanoplates synthesized at 280 °C are determined to be 6.002 Å (*a*), 3.793 Å (*b*), and 14.477 Å (*c*), which are comparable with the values reported for bulk $CuSbS_2$.[15] An expanded portion of XRD peaks in region of 28°−31° for nanoplates of various thicknesses is shown in Figure 2b. With increasing growth temperature, the peaks become sharper with formation of a distinct doublet. In addition, changes in the full width at half-maximum of XRD peaks of nanoplates grown at different temperatures clearly indicate increase in layer thickness with increasing synthesis temperature. The crystal structure of orthorhombic $CuSbS_2$ is shown in Figure 2c. It consists of covalently bonded quadruple layers bound together by van der Waals forces, which connect Sb and S with a distance of ~3.115 Å. The average elemental composition of the nanoplates and mesobelts has been determined using energy dispersive X-ray spectroscopy (EDX) with the samples coated on carbon tape attached to SEM stubs. The results yield a composition close to a ratio of 1:1:1.95 (copper:antimony:sulfur) for both nanoplates and mesobelts. These quantitative composition values are obtained from different locations, each consisting of a large number of particles (Figure 2e).

Nanoplates by Bottom-Up Approach. The morphology, size, and thickness of the nanocrystals obtained using the bottom-up approach have been investigated using a transmission electron microscope (TEM). TEM images in Figure 3a−d show plate-like morphology for all growth temperatures. Close observation of the images reveals a clear trend of

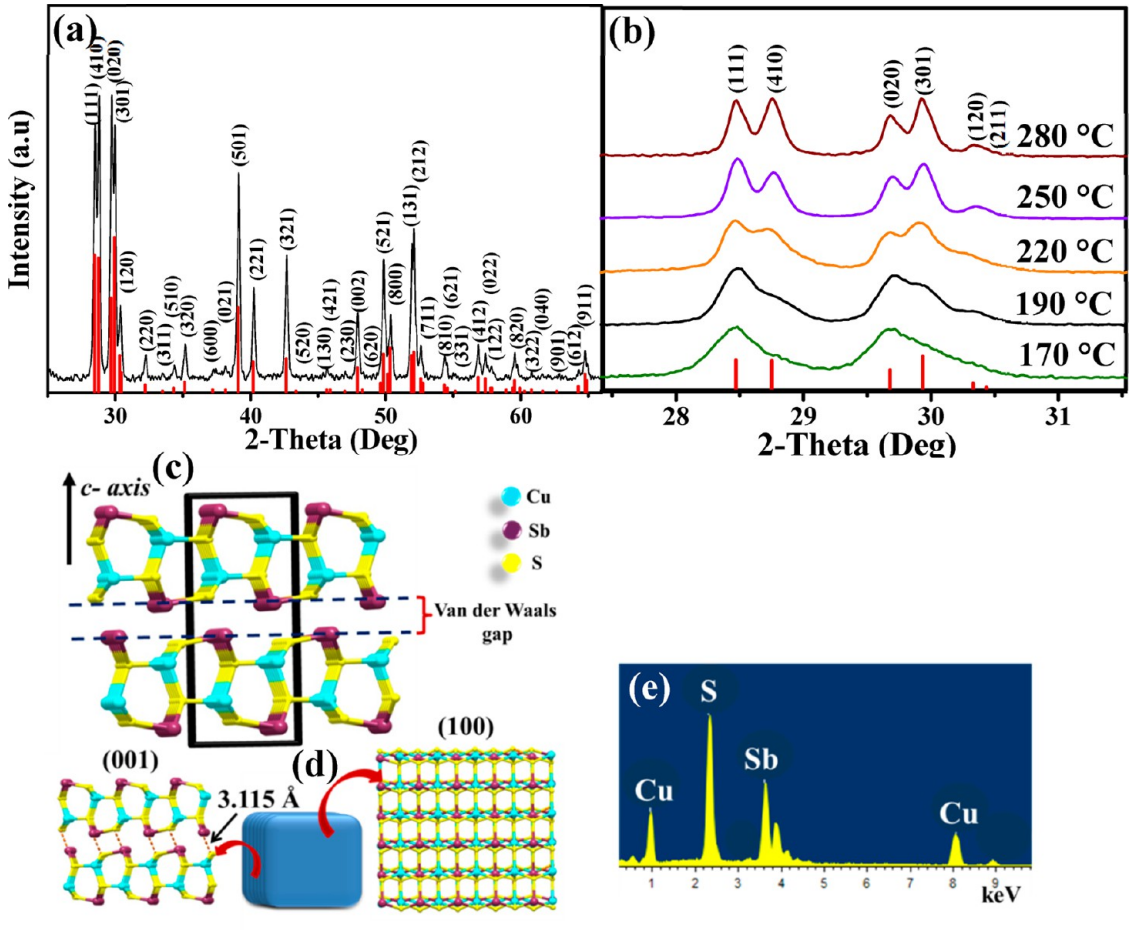

Figure 2. (a) Powder X-ray diffraction pattern of $CuSbS_2$ nanoplates grown at 280 °C for 30 min. (b) Expanded portion of powder X-ray diffraction patterns of nanoplates grown at different temperatures for 30 min. (a) Crystal structure of $CuSbS_2$ showing the van der Waals gap between two quadruple layers. (d) Schematic illustrating the different growth directions of nanoplates. (e) SEM-EDX spectrum of $CuSbS_2$ nanoplates grown at 220 °C.

dx.doi.org/10.1021/ja411748g | J. Am. Chem. Soc. 2014, 136, 1587−1598

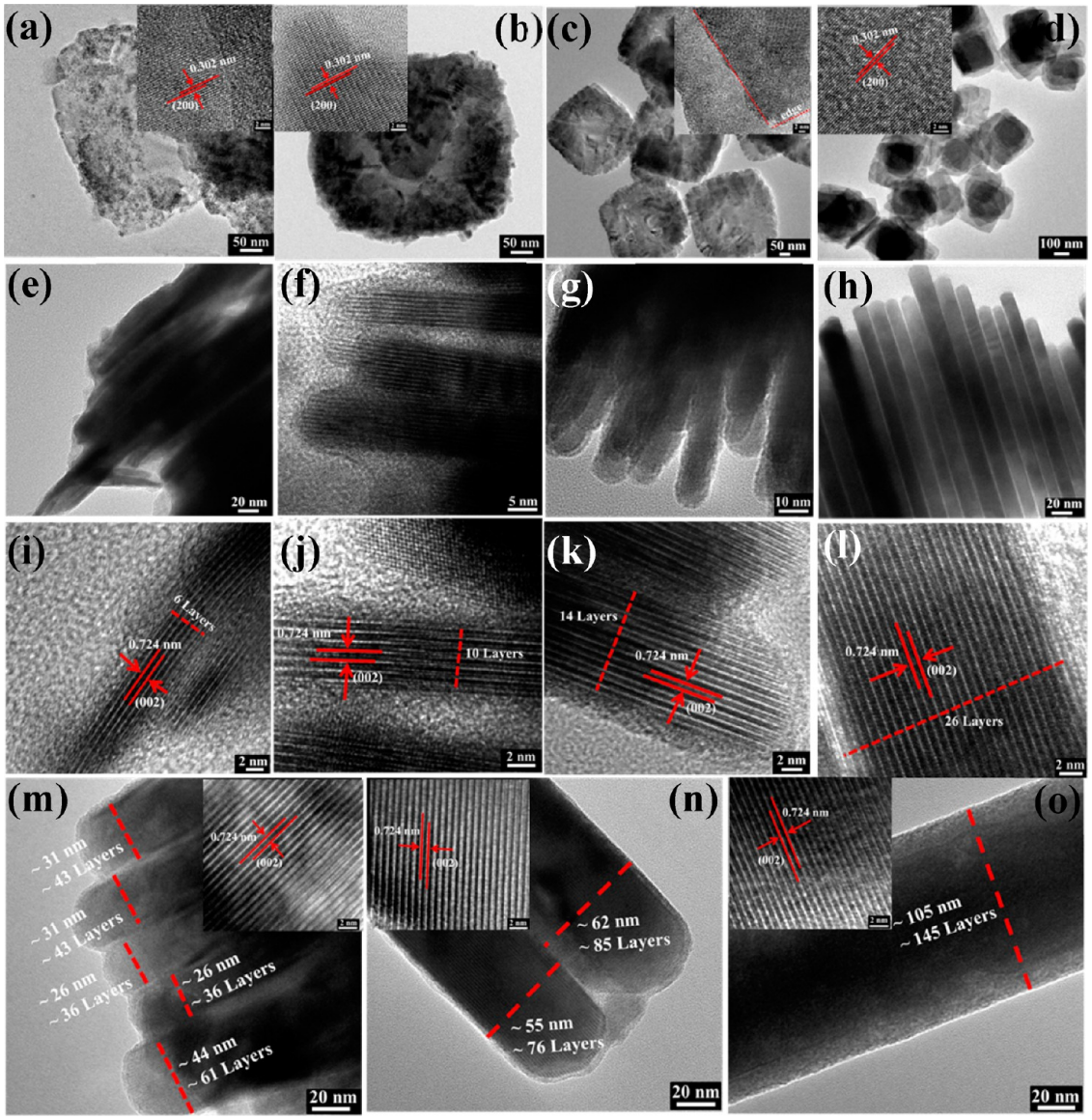

Figure 3. (a–c) Top-view TEM images of nanoplates grown at 170 °C for 10, 15, and 30 min, respectively (insets show the corresponding HRTEM images). (d) Top-view TEM images of nanoplates grown at 190 °C for 30 min. (e–h) Side-view TEM images of nanoplates grown at 170 °C for 10, 15, and 30 min and at 190 °C for 30 min. (i–l) Side-view HRTEM images of nanoplates. (m–o) Side view TEM images of nanoplates grown at 220 °C, 250 and 280 °C for 30 min, respectively (insets show corresponding HRTEM images).

decreasing electron beam transparency of the nanoplates with increasing growth time, consistent with thicker growth. The average lateral size of the nanoplates synthesized at 170 °C are 450 ± 20 nm for 10 min, 455 ± 15 nm for 15 min, and 400 ± 25 nm for 30 min of growth; and for the plates obtained at temperatures 190–280 °C between 300 ± 20 nm and 335 ± 25 nm for 30 min. The images also clearly indicate that the plates are composed of several stacks of layers with distinct plate edges and intermittent Moiré patterns (TEM image showing Moiré patterns is given in Figure S2). HRTEM images of the surface of plates in insets to Figure 3a–d show well-defined lattice fringes with an average lattice distance of 0.302 ± 0.003 nm, corresponding to the (200) planes of orthorhombic $CuSbS_2$ phase (considering *c*-axis as the long axis of the unit cell).

The thickness of the plates synthesized at 170 °C, as measured from TEM images in Figure 3e–o, is found to be 4.0 ± 0.8 nm for 10 min, 7.0 ± 0.7 nm for 15 min, and 10.0 ± 0.5 nm for 30 min, which corresponds to 6, 10, and 14 layers, respectively. Furthermore, TEM images of the plates obtained in the temperature range of 190–280 °C for 30 min reaction time show an increase in thickness from 19 ± 1 nm to 105 ± 3 nm. HRTEM images of the edges of the plates exhibit lattice fringes with an average lattice distance of 0.724 ± 0.002 nm, corresponding to the (002) planes along [001] growth direction. These observations clearly indicate that increasing the reaction time and temperature facilitates growth of nanoplates along the *c*-axis direction, which is to be expected since the process is driven by van der Waals interactions. The details of the samples prepared under different process conditions are provided in Table S1 and their composition analysis in Table S2

Mesobelts by Hybrid Bottom-Up-Top-Down Approach. As mentioned earlier, for obtaining very thin layers of $CuSbS_2$ we carried out a hybrid bottom-up-top-down approach. Using this approach, belt-like mesostructures with

dx.doi.org/10.1021/ja411748g | J. Am. Chem. Soc. 2014, 136, 1587–1598

lengths of about 10 μm are first grown and are then exfoliated to form mono- and few layers by lithium intercalation and sonication processes. In our synthesis we used a mixture of 1-DDT and *t*-DDT for the formation of mesobelt-like structures considering the fact that thiol molecules generally stabilize elongated structures, as has been previously observed in a number of other studies.[28,29] SEM images of mesobelts obtained at 250 °C using this method are shown in Figure 4a,b,d,e. The images show nearly uniform morphology of

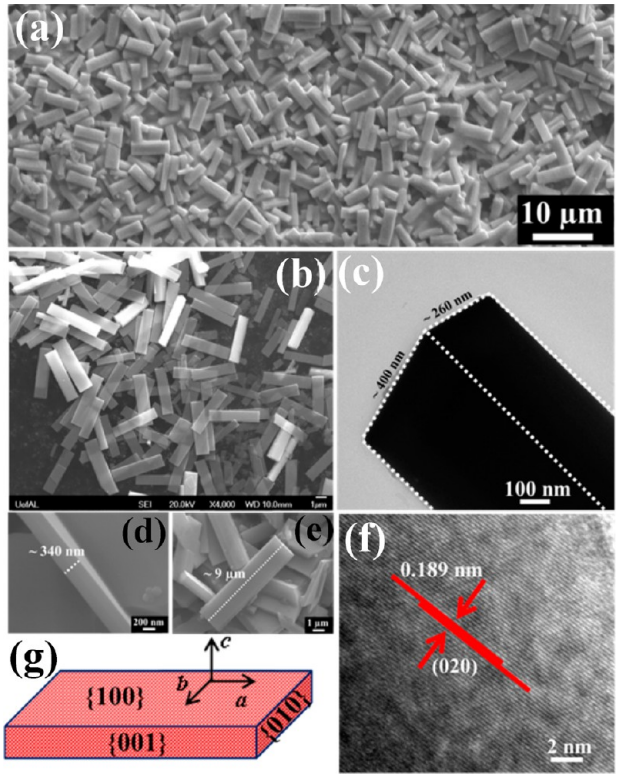

Figure 4. (a) and (b) SEM images showing mesobelt morphology of $CuSbS_2$. (c) TEM image of mesobelts grown at 250 °C for 30 min. (d) and (e) Magnified images of mesobelts. (f) HRTEM image of a mesobelt. (g) Schematic illustrating the growth directions of mesobelts.

mesobelts for the entire sample. The length of the mesobelts ranges between 9 and 10 μm, with thickness in the range of 250−350 nm and width of about 400 nm.

Attempts to reduce the thickness of the mesobelts by decreasing the reaction temperatures to 220 and 190 °C produced predominantly irregular structures (Figure S3), and temperatures below 190 °C resulted in the formation of copper sulfide impurity phase.

The observed morphology is intriguing, and to better understand the anisotropic growth behavior, we carried out time-dependent TEM studies as discussed later in the Growth Mechanism of Mesobelts section. For obtaining information about the growth direction of mesobelts, we performed HRTEM analysis by imaging the edge of the mesobelts. The image in Figure 4f exhibits lattice fringes with a separation distance of 0.189 nm, corresponding to the (020) planes of orthorhombic $CuSbS_2$. However, lattice image from the top and side surfaces could not be obtained because the thickness of the mesobelts is not penetrable by the electron beam. Based on comparison of the HRTEM image with the crystal structure of $CuSbS_2$, possible growth orientation of the mesobelts is illustrated in Figure 4g.

The mesobelts prepared at 250 °C are used for Li-ion intercalation in hexane, and the exfoliation process is carried out in water. In this process, lithium ions are intercalated between the quadruple layers of $CuSbS_2$, which are separated by weak van der Waals forces. The intercalated lithium ions in water produce lithium hydroxide and hydrogen gas, which helps split the mono- and few layers of $CuSbS_2$ during the sonication process.[30] We observed that the uniformity and thinness of the layers are strongly influenced by the amount of *n*-BuLi used for intercalation and the sonication duration. A schematic of the intercalation and exfoliation processes is provided in Figure 5a. SEM images of the exfoliated mono- and

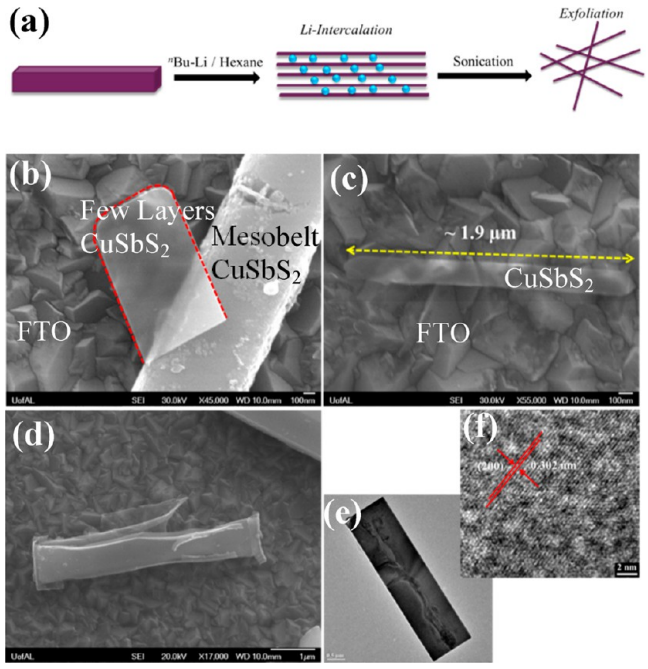

Figure 5. (a) Schematic representation of Li intercalation and exfoliation of $CuSbS_2$ mesobelts to form thin layers. (b) and (c) SEM images of thin layers exfoliated from $CuSbS_2$ mesobelts. (d) SEM image shows peeling-off of layers from a $CuSbS_2$ mesobelt. (e) TEM image of a $CuSbS_2$ exfoliated mesobelt. (f) HRTEM image of exfoliated layer.

few layers of $CuSbS_2$ dispersed on a fluorine-doped tin oxide (FTO) substrate are shown in Figure 5b−d. The images show transparent layers (apparent from the visibility of background FTO grain structure through the layers) that mostly retain their parent morphology. The largest layers obtained by this method have a length of about 1.9 μm, as can be seen in Figure 5c. SEM and TEM images (Figure 5d,e) of partially exfoliated mesobelts show peeling off of the surface layers, confirming that the layers are held together through van der Waals bonding along the *c*-axis direction. HRTEM image of the surface of the layers in Figure 5f shows lattice planes with interplanar distance of 0.302 nm, corresponding to (200) plane of $CuSbS_2$. Furthermore, the image shows evidence of some structural damage on the surface of the layers caused by the Li-ion intercalation and exfoliation process. This type of structural damage from exfoliation has previously been noted for a number of other layered materials, including graphene.[31,4] Interestingly, the exfoliated layers are dispersible in water and remain suspended for up to 2 days. It

dx.doi.org/10.1021/ja411748g | *J. Am. Chem. Soc.* 2014, 136, 1587−1598

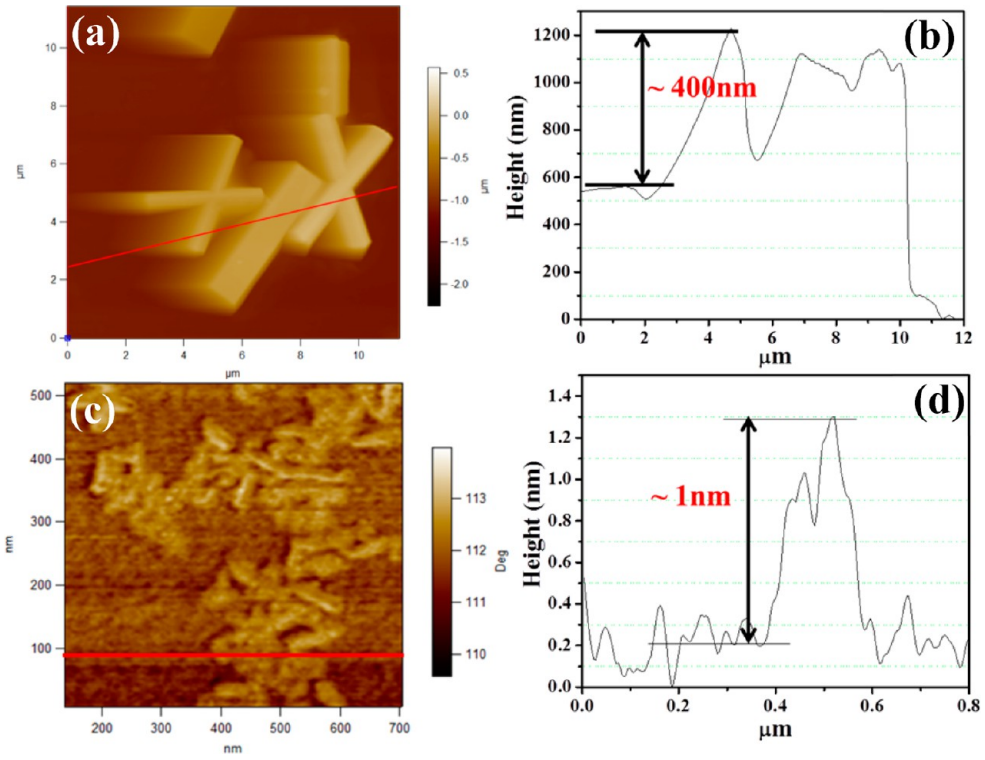

Figure 6. (a) and (c) AFM images of mesobelts and exfoliated layers. (b) and (d) Corresponding height profile of the scans shown in the AFM images.

has been reported that the intercalation of lithium ion in copper-containing ternary spinels facilitate replacement of copper ions by lithium ions.[32−34] In order to ensure that copper ion replacement by lithium ion is not occurring in the layered structure $CuSbS_2$, we have analyzed the exfoliated layers using powder X-ray diffraction. The XRD pattern in Figure S4b exhibits broad low-intensity diffraction peaks at positions similar to the XRD pattern of the parent mesocrystals confirming retention of the original orthorhombic $CuSbS_2$ structure. The broadness of diffraction peaks indicates loss of long-range structural order in the crystallites lattices as expected. The drastic change in X-ray diffraction peaks intensity is due to the thinness and possible structural deformation during the exfoliation process, as also witnessed in HRTEM image (Figure 5f). SEM-EDX analysis was carried out to further confirm the stoichiometry of exfoliated layers (Figure S5). EDX data of the samples before and after Li-ion intercalation and exfoliation process are given in Tables S3 and S4, respectively.

The results suggest that the relative ratio of copper, antimony, and sulfur after exfoliation is nearly 1:1:2, preserving the original mesobelts stoichiometric ratio. The XRD and EDX results do not provide evidence for lithium ion replacement of copper ions in layered structured $CuSbS_2$. However, the possibility of a small replacement of copper ions with lithium ions cannot be ruled out and can only be confirmed by detailed electron energy loss spectroscopy (EELS) mapping analysis.

To accurately determine the number of layers obtained by exfoliation, we have performed noncontact mode atomic force microscopy (AFM) analysis (Figure 6). The AFM image in Figure 6a shows smooth mesobelts (before exfoliation) with some cross-linked structures. A line scan (Figure 6b) across the mesobelts indicates a thickness of about 400 nm, which is close to the value obtained from SEM and TEM analysis.

The image in Figure 6c for the exfoliated sample on Si/SiO_2 wafers shows smooth, uniform rod-like structures that are considerably smaller than the parent mesobelts. The cross-sectional height profile in Figure 6d reveals that the thickness of these $CuSbS_2$ layers is ∼1 nm, which is close to monolayer thickness of $CuSbS_2$ (half unit cell length along *c*-axis direction is 0.724 nm). Besides monolayers, a few thicker layers are also observed in the AFM image.

Growth Mechanism of Mesobelts. To understand the growth mechanism of the anisotropic mesostructures, we have carried out time-dependent TEM analysis of samples taken out from the reaction mixture at different time intervals. The TEM images obtained at different time intervals are shown in Figure 7a−l. Careful analysis of the images provides important insights regarding the intermediates that lead to the formation of mesobelts. During the initial stage, coalescence of individual randomly shaped nanoparticles is observed along with smaller nanodots of size ∼2 nm that appear to form two-dimensional (2D) sheet-like structures (Figure 7a). Coalescence of these nanosheets leads to the formation of uniform plate-like structures displaying clear nanosheet edges, as observed in Figure 7b. Furthermore, the TEM image in Figure 7c shows that once the vertical attachment attains a specific shape, the nanosheets grow out laterally. These images provide clear evidence of the competition between van der Waals forces favoring the vertical growth and uncompensated dangling bonds forcing the nanosheets to grow laterally. At this early stage of growth, the nanosheets are thin and tend to fold and buckle up through a homoepitaxial process to form prolate-shaped structures (Figure 7d,e). The folding up of nanosheets has previously been noted during the growth of other layered materials.[35] In the next step, the small prolate-shaped particles attach to each other through a common crystallographic face, creating fully formed 3D irregular nanocrystals, as observed in

dx.doi.org/10.1021/ja411748g | J. Am. Chem. Soc. 2014, 136, 1587−1598

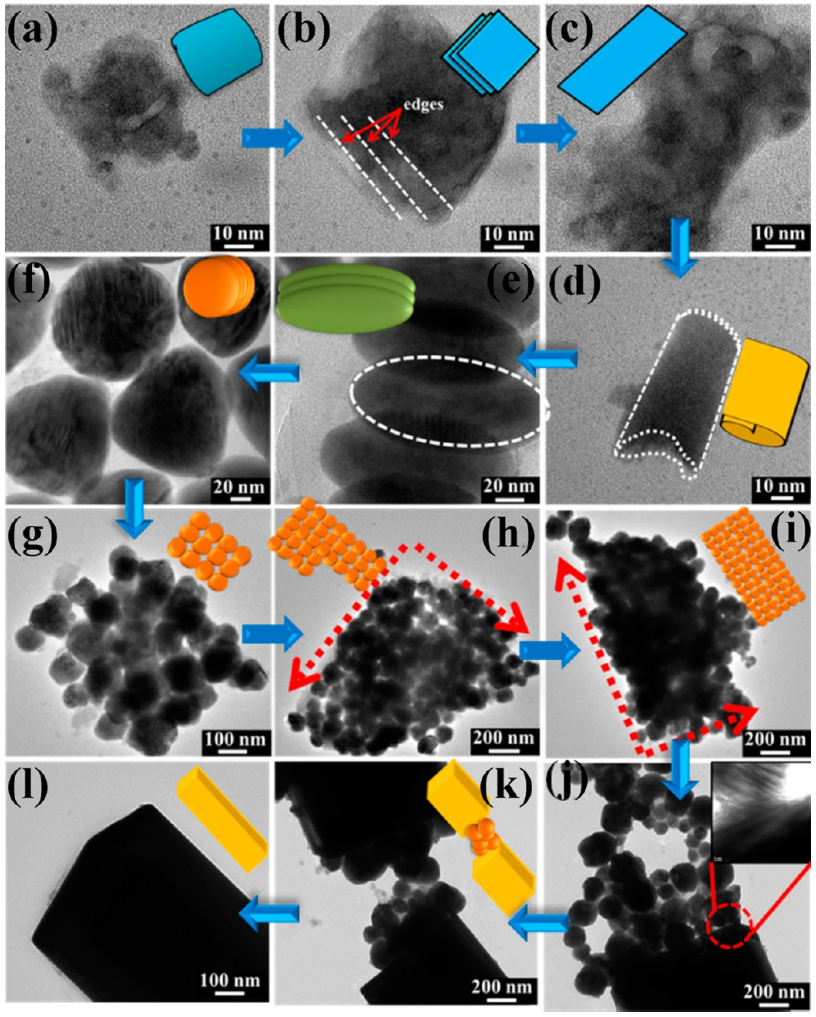

Figure 7. (a–l) TEM images showing the various intermediate morphologies involved in the formation of mesobelts at 250 °C . Insets show schematics of intermediate morphologies. Inset to (j) shows magnified TEM image of circled area. Arrows (blue) are indicated for guidance of the eye.

Figure 7f. Once these structures are formed, they bond together through a likely nonclassical crystal growth mechanism to attain the stable mesobelt structure. The TEM images with details of irregular-shaped nanoparticles attaching together and growing anisotropically to form mesobelt-like structures are shown in Figure 7g–l.

In addition, inset to Figure 7j shows a representative high magnification TEM image of the circled area in Figure 7j, providing evidence of nanocrystals starting to attach to the surface of partially grown mesobelts during the oriented attachment crystal growth process.

A pictorial representation of the intermediates formed at different time intervals is shown in Figure 8a. It depicts the temporal transformation of nanocrystals from one shape to another eventually leading to the formation of mesobelts (colors indicate different stable shapes). SEM image in Figure 8b shows a large number of irregularly shaped nanocrystals, which are isolated after 10 min of reaction at 250 °C. TEM images with stepwise magnification of one of the irregularly shaped nanocrystal are shown in Figure 8c–f. From these images, it can be observed that the nanocrystals are composed of crystalline (confirmed by well-defined lattice planes) prolate-shape nanocrystals. Further insight into the crystallographic orientation of the nanostructures is provided by the HRTEM image in Figure 8f. The image shows a highly crystalline stack with lattice fringes. The distance between the parallel lattice planes is about 0.302 nm, corresponding to the (200) planes of orthorhombic $CuSbS_2$, which is consistent with the distances measured for the exfoliated layers. This confirms that the prolate nanocrystals with irregular shape structures are formed by folding up of initially grown nanosheets. Overall, the TEM and SEM images provide definitive insights regarding formation of the mesobelts through initial nucleation and growth of nanosheets, folding and buckling up of nanosheets by van der Waals homoepitaxy, attachment of prolate shape nanocrystals, restructuring and aggregation of irregular nanocrystals, and eventual ripening to form the mesobelts.

It is interesting to note that when the reaction was carried out using sulfur in OLA as the sulfonating agent, only nanoplates were obtained, whereas the same reaction using a mixture of 1-DDT and *t*-DDT produced mesobelt-like structures. In the case of sulfur in OLA, when the sulfonating agent was injected into the reaction vessel containing OLA suspension of metal precursors, the concentration of sulfur is abruptly diluted leading to production of fewer number of reactive nuclei and further lateral growth through Ostwald ripening process to produce nanosheets. Once the initial nanosheets with definite lateral dimensions are formed, they

dx.doi.org/10.1021/ja411748g | *J. Am. Chem. Soc.* 2014, 136, 1587–1598

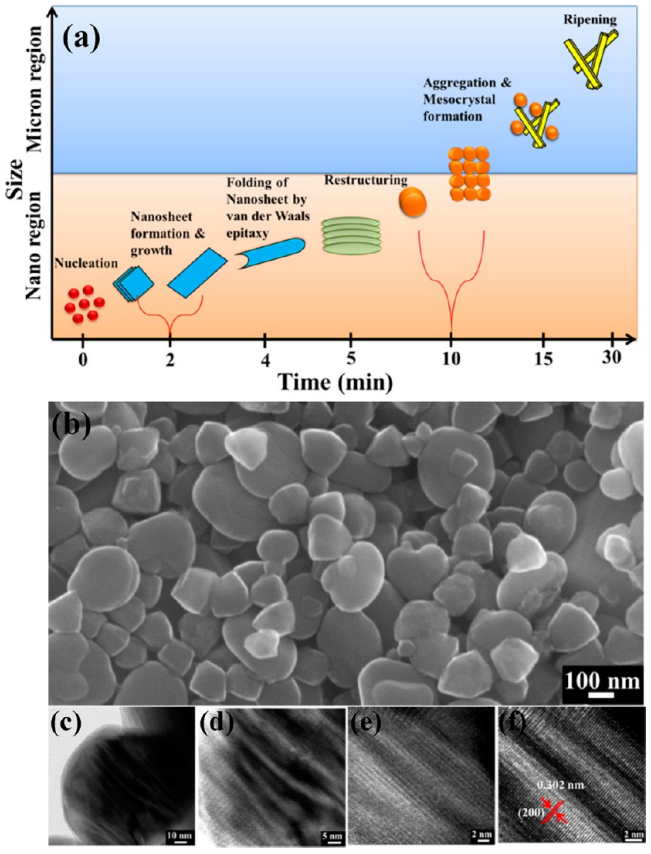

Figure 8. (a) Pictorial representation of intermediates observed at different stages of the growth of mesobelts (colors indicates different shapes). (b) SEM image of irregular shaped nanocrystals. (c) TEM image of one of the irregular-shaped nanocrystal showing that it is composed of folded plates. (d–f) HRTEM images of irregular-shaped nanocrystal.

continue to grow vertically, which is facilitated by van der Waals attractions. But the reaction using a mixture of 1-DDT and *t*-DDT, produces CuSb-thiol or Cu-thiol and Sb-thiol coordination complexes at the initial stage and is followed by gradual decomposition of complexes leading to formation of reactive nuclei. The coordination complexes of copper and antimony are more likely to be formed with *t*-DDT, since it is a stronger nucleophile than 1-DDT, which leaves 1-DDT to act as a capping agent. Once the reactive nuclei are formed, they tend to grow laterally to form anisotropic nanosheets unlike the other case with S/OLA.

In the layered structure of $CuSbS_2$, [100] and [010] crystallographic directions are terminated with atoms that have unsaturated dangling bonds making them high-energy surfaces. These high-energy surface atoms make partial coordination bonds with capping ligands, in this case, most likely with thiol molecules to reduce the surface energy. With continued heating of the reaction mixture, C–S bonds tend to break, which facilitates bond formation with copper and antimony. However, as the lateral dimensions of the nanosheets increase, the van der Waals attraction along the *c*-axis also increases and eventually exceeds the surface energies along *a*- and *b*-axes. This makes the nanosheets fold up and attach through homoepitaxy to form a prolate-like structure. Subsequently these prolate-like structures rotate and orient to form mesocrystals via irregular intermediates assisted by the OLA and dodecanethiol capping agents. The formation of mesocrystals through oriented attachment crystal growth mechanism has been documented in a number of other cases.[36,37]

Optical Properties. UV–vis-NIR absorption spectra of toluene dispersion of nanoplates with different thicknesses are shown in Figure 9a. Absorption spectrum of nanoplates with 6

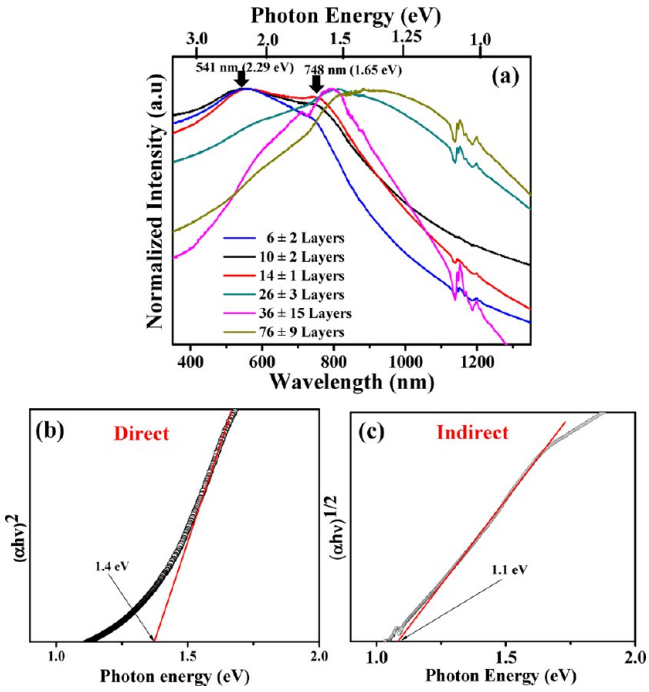

Figure 9. (a) UV–vis-NIR absorption spectra of nanoplates with different thickness (noisy features near 1150 nm are due to grating change). Extrapolation of the absorption spectra of 6 ± 2 layers thick nanoplates in the band edge region for determination of (b) direct and (c) indirect band gaps.

layer thickness synthesized at 170 °C for 10 min showed a broad absorption peak at 541 nm (2.29 eV) and a shoulder at 748 nm (1.65 eV). As the thickness of nanoplate is increased from 6 ± 2 layers to 14 ± 1 layers, the absorption shoulder at 748 nm becomes more prominent with its intensity increasing to nearly the same level as the peak at 541 nm. The dual absorption features for $CuSbS_2$ nanoplates can be attributed either to the presence of both direct and indirect transitions or due to spin–orbit coupling as in the case of molybdenum sulfide.[38] Interestingly, these transitions have not been reported for bulk or nanobricks of $CuSbS_2$.[12,13] Detailed optical and theoretical studies will be required for exact assignment of these transitions. The increase in intensity of the low-energy peak is significantly pronounced for the nanoplates with thickness from 26 ± 3 to 76 ± 9 layers, which were grown at temperatures of 190–250 °C (Figure 9a). The optical spectrum of nanoplates with 26 ± 3 layers shows a dual absorption behavior with a hump at 585 nm (2.12 eV) and a broad peak at 798 nm (1.55 eV), which are red-shifted from the absorptions observed for the nanoplates thinner than 14 layers. When the thickness of the nanoplates is increased (76 ± 9 layers) by increasing growth temperature to 250 °C, the hump at 585 nm diminishes significantly, and the peak at 798 nm shifts to 908 nm (1.36 eV). $CuSbS_2$ has been theoretically predicted to be an indirect band gap material with a difference between direct (~1.7 eV) and indirect (~1.6 eV) band gaps of ~0.1 eV.[11,39] However,

dx.doi.org/10.1021/ja411748g | J. Am. Chem. Soc. 2014, 136, 1587–1598

most experimental studies report the material to have a direct band gap (~1.4 eV).[12] Band gap values for the nanoplates have been obtained by plotting $(Ah\nu)^2$ versus $h\nu$ for direct and $(Ah\nu)^{1/2}$ versus $h\nu$ for indirect gap (A = absorbance, h = Planck's constant, and ν = frequency) and extrapolating the linear portion of the spectrum in the band edge region.[40] In our case, the direct and indirect band gap values are determined to be 1.40 and 1.1 eV, respectively, for 6 ± 2 layers thick nanoplates (Figure 9b,c). The direct band gap is close to the band gap value reported for nanobricks of $CuSbS_2$.[12]

It is important to note that the estimated band gap from the absorption spectra decreases systematically with increasing thickness of the nanoplates, indicating a thickness-dependent quantum confinement effect.

Optical spectra of exfoliated $CuSbS_2$ layers are shown in Figure 10a. The spectrum for the monolayers shows a long tail with a hump around 500 nm. The band gap values (Figure 10b,c) obtained from extrapolating the linear portion of the spectrum are 1.9 eV (direct) and 1.5 eV (indirect). Comparing the optical spectrum of exfoliated layers with those of the nanoplates (absorption measurement on mesobelts sample was not possible due to its poor dispersibility), there is absence of the dual absorption behavior along with a higher band gap value, indicating a large quantum confinement effect as confirmed from band structure calculation discussed in the next section. The large difference in the band gap value for exfoliated layers in comparison with 6 ± 2 layer thick nanoplates may also partly be due to lithium-induced strain and structural defects during the exfoliation process.

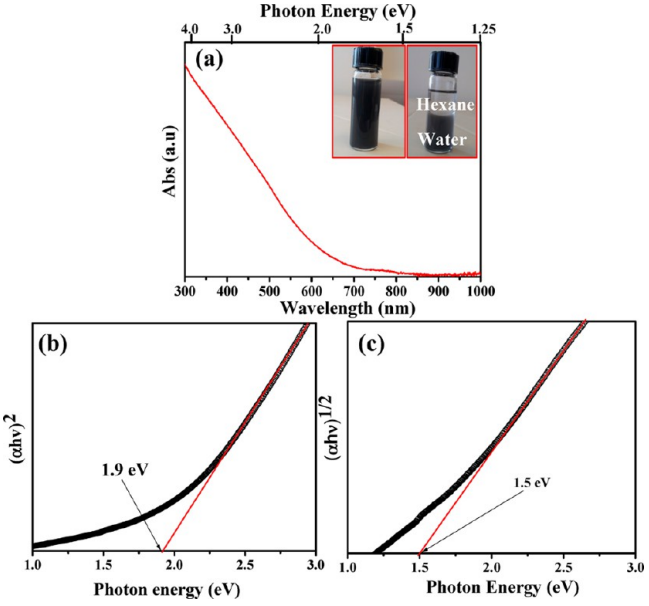

Figure 10. (a) UV−vis-NIR absorption spectra of exfoliated layers of $CuSbS_2$ (inset shows photographs of exfoliated monolayers dispersed in water). Extrapolation of the absorption spectra in the band edge region for determination of (b) direct (c) indirect band gaps for the exfoliated layers.

Band Structure Calculations. The bulk electronic structure of $CuSbS_2$ has been previously studied within both PBE and HSE06,[39,11] and we refer the reader to these references for a more thorough discussion of the bulk electronic structure. Here we focus on the changes that arise with the introduction of a surface, particularly in the monolayer structure (in which we take half of the primitive cell to be a single layer). The 2D TMDCs, of which MoS_2 is the most famous example, exhibit an increasing band gap with decreasing number of layers, accompanied by an indirect-to-direct gap transition in the limit of a single layer. In a monolayer of MoS_2, the p_z orbitals of the surface S ions no longer feel the Coulomb repulsion of adjacent S atoms across the van der Waals gap, lowering the energy of these states and consequently moving the valence band maximum to the Γ point.[41] It has been reported that a similar situation arises in monolayers of SnS, although in that case there is no indirect-to-direct transition.[42] Again, the elimination of interlayer Coulomb repulsion seems to be the key factor, although it is claimed that a reduction in (in-plane) hybridization also contributes.

The crystal structure of $CuSbS_2$ is somewhat more complex than that of SnS or the TMDCs, and assuming an absence of surface reconstruction or defects, the (001) faces will be terminated in both S and Sb ions. Therefore, it is not only the occupied S p_z but also the unoccupied Sb p_z states that will lower their energy in response to the lack of electrostatic repulsion from neighboring layers. This can be seen in both the density of states plots (Figure 11) and the band structures (Figure 12). In Figure 11, one clearly sees a set of states (containing four electrons, two for each of the Sb p_z orbitals)

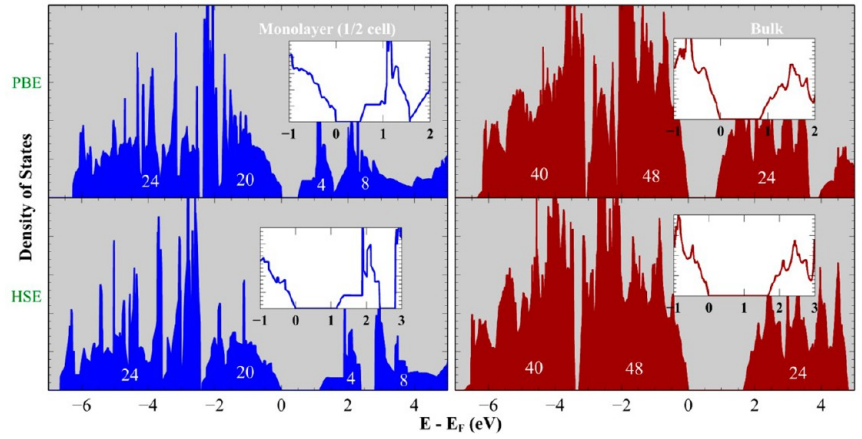

Figure 11. Total density of states for $CuSbS_2$ within PBE and HSE (top and bottom panels, respectively) for the monolayer (left panels) and bulk (right panels) structures. The number of electrons in a given group of states, as computed from the integrated DOS, is indicated in white. (insets) Close-up of the region around the Fermi energy.

dx.doi.org/10.1021/ja411748g | J. Am. Chem. Soc. 2014, 136, 1587−1598

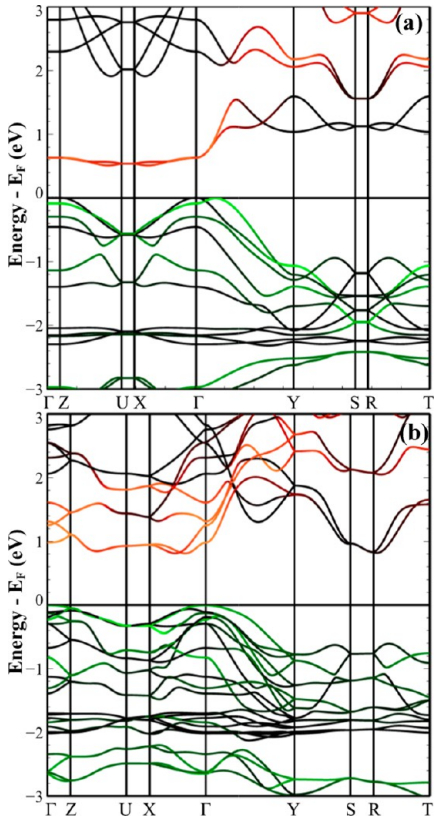

Figure 12. Electronic band structure for (a) monolayer and (b) bulk $CuSbS_2$. S p_z character is indicated by the color green (with light green having the most and black the least), and Sb p_z character in the conduction bands is indicated by increasing "warmth" of the color red.

that has split off from the main body of conduction states, partially in the PBE calculations and fully in HSE06. Likewise, Figure 12 shows that additional S $p_{x/y}$/Cu d states (largely unaffected by the removal of neighboring layers) have joined the mostly S p_z state at the top of the valence band. So, we see that, although the energy of the valence band maximum is reduced in the monolayer, the concomitant reduction in energy of the conduction band minimum negates any resulting increase in the fundamental gap. However, we also find that the lowest-lying Sb p_z states are almost dispersionless, being localized to the surface Sb ions. As a result, they should show up at most as an extended tail in the absorption curve (the computed curves can be found in Figure 13), while the higher-energy vertical VBM-Sb p_x/p_y transitions become more important. Indirect transitions into other Sb p states (e.g., Γ−Y) are also predicted to increase slightly in energy. To further compare the transport properties of the bulk and monolayer systems, we compute the effective conduction electron masses, as seen in Table 1. In the monolayer, we do not consider the symmetry lines along the *z*-axis, and we compute the effective masses of both the localized Sb p_z bands (indicated by (surf.)) and the other more dispersive Sb bands. Unsurprisingly, in the monolayer system, the localized conduction electrons tend to be rather "heavy," while the higher-energy Sb bands are generally quite light. The monolayer bands from Γ−Y and Y−S have less p_z character and consequently more closely match their counterparts in the bulk system.

Table 1. Computed Effective Conduction Electron Masses for Bulk and Monolayer $CuSbS_2$[a]

bulk		monolayer	
	m^* (m_e)		m^* (m_e)
Γ−Z	2.93 (Γ)	X−Γ	1.3 (surf.)
Z−U	0.59		0.12 (X)
U−X	3.8 (U)		1.3 (Γ)
X−Γ	0.54	Γ−Y	0.22 (surf., Γ)
Γ−Y	0.20 (Γ)		2.0 (surf., Y)
Y−S	0.27		0.76 (Y)
S−R	0.51 (R)		0.21−0.32
R−T	0.29	Y−S	1.9 (surf., S,Y) 0.18 (S)

[a]When the local band minimum occurs at a symmetry point, this is indicated by placing the name of this point in parentheses after the effective mass.

The computed absorption curves for the bulk and monolayer structures seem to incorporate some features of the observed behavior. The bulk curve shows two peaks at around 2.3 and 2.6 eV. Given the larger optical band gap predicted by the HSE curve (~1.8 eV compared to ~1.4 eV in the experimental curve (Figure 9b), these peaks can be reasonably equated with those appearing at ~1.65 and ~2.3 eV. Likewise, discounting the

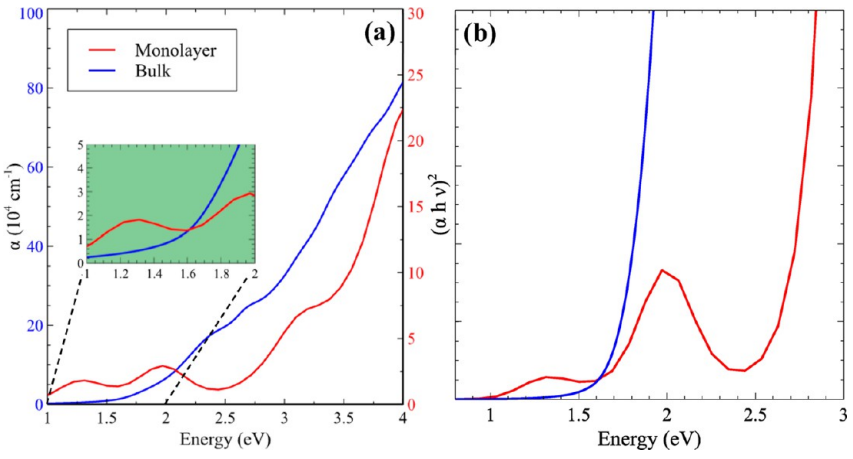

Figure 13. (a) Absorption curves from HSE06 for bulk (blue) and monolayer (red) structures. (inset) Absorption in visible range between 1 and 2 eV. (b) Estimation of the (direct) optical gap via the energy intercept of the $(\alpha h\nu)^2$ vs $h\nu$ curve.

dx.doi.org/10.1021/ja411748g | J. Am. Chem. Soc. 2014, 136, 1587−1598

lower energy peaks arising from the localized surface states, there is only a single peak at about 3.1 eV in the monolayer curve. Again, the HSE optical gap is considerably larger than the experimental one (~2.6 versus ~1.9 eV), but we do find a single peak and a broad tail in the low-energy absorption curve, in agreement with the measured data. Although the quantitative agreement is lacking, the HSE electronic structure provides a reasonable quantitative picture of the $CuSbS_2$ monolayer.

CONCLUSION

We have developed simple approaches for the synthesis of mono-, few-, and multiple layers of $CuSbS_2$. $CuSbS_2$ nanoplates with thickness from 6 ± 2 layers to several layers are obtained by a colloidal bottom-up approach using S/OLA as sulfur source. Hybrid bottom-up-top-down approach is carried out for formation of monolayers of $CuSbS_2$. Here, $CuSbS_2$ mesobelts are initially synthesized using a mixture of 1-DDT and *t*-DDT as sulfonating agents, and then these are exfoliated by Li-ion intercalation and sonication process to obtain monolayers. TEM studies to understand the mesobelts growth mechanism suggest lateral growth of nanocrystals at the initial stage to form nanosheets as a primary structure, followed by subsequent nanosheets fold up and attach through homoepitaxy to form prolate-like secondary structures. Eventually, these prolate-like structures form mesocrystals by oriented attachment crystal growth through irregular intermediates assisted by the OLA and dodecanthiol. Optical measurements of monolayers show a significant increase in band gap value than that of nanoplates, suggesting a thickness-dependent quantum confinement effect. The electronic structures of mono- and multiple layers of $CuSbS_2$ using the hybrid functional method (HSE 06) predict that the monolayer exhibits noticeably different properties from the multilayered or bulk system, with a markedly increased band gap that is however compromised by the presence of localized surface states. These are predominantly composed of the energetically favorable Sb p_z states, which break off from the rest of the Sb p states that would otherwise be the top of the gap. The computed absorption spectra for the monolayer and bulk indicate gaps of around 2.5 and 1.6 eV, respectively, with additional peaks at lower energies in the former due to the split-off Sb states. Our findings suggest that the optical and electrical properties of $CuSbS_2$ can be tuned by reducing its thickness down to monolayer. However, the applicability of monolayer $CuSbS_2$ for practical devices can be gauged only after determining the transport properties, which is being pursued, and the results will be reported elsewhere.

ASSOCIATED CONTENT

Supporting Information

TEM image showing Moire pattern, SEM images, XRD patterns, EDX data. This material is available free of charge via the Internet at http://pubs.acs.org.

AUTHOR INFORMATION

Corresponding Authors

agupta@mint.ua.edu
kramasamy@mint.ua.edu

Present Address

[‖]German Research School for Simulation Science, Jülich, Germany-52425.

Notes

The authors declare no competing financial interest.

ACKNOWLEDGMENTS

We thank Dr. Matthias Althammer for the AFM measurements and Dr. Thomas Vaid for allowing us to use his UV−vis-NIR instrument. This research was supported by the U.S. Department of Energy, Office of Basic Energy Sciences, Division of Materials Sciences and Engineering under award no. DE-FG02-08ER46537

REFERENCES

(1) Bertolazzi, S.; Krasnozhon, D.; Kis, A. *ACS Nano* **2013**, *7*, 3246−3252.
(2) Novoselov, K. S.; Geim, A. K.; Morozov, S. V; Jiang, D.; Zhang, Y.; Dubonos, S. V; Grigorieva, I. V; Firsov, A. A. *Science.* **2004**, *306*, 666−669.
(3) Nair, R. R.; Wu, H. A.; Jayaram, P. N.; Grigorieva, I. V; Geim, A. K. *Science* **2012**, *335*, 442−444.
(4) Xu, M.; Liang, T.; Shi, M.; Chen, H. *Chem. Rev.* **2013**, *113*, 3766−3798.
(5) Ataca, C.; Sahin, H.; Ciraci, S. *J. Phys. Chem. C* **2012**, *116*, 8983.
(6) Koski, K. J.; Cui, Y. *ACS Nano* **2013**, 3739−3743.
(7) Wang, Q. H.; Kalantar-Zadeh, K.; Kis, A.; Coleman, J. N.; Strano, M. S. *Nat. Nanotechnol.* **2012**, *7*, 699−712.
(8) Seo, J.; Jang, J.; Park, S.; Kim, C.; Park, B.; Cheon, J. *Adv. Mater.* **2008**, *20*, 4269−4273.
(9) Splendiani, A.; Sun, L.; Zhang, Y.; Li, T.; Kim, J.; Chim, C.-Y.; Galli, G.; Wang, F. *Nano Lett.* **2010**, *10*, 1271−5.
(10) Eda, G.; Yamaguchi, H.; Voiry, D.; Fujita, T.; Chen, M.; Chhowalla, M. *Nano Lett.* **2011**, *11*, 5111−5116.
(11) Dufton, J. T. R.; Walsh, A.; Panchmatia, P. M.; Peter, L. M.; Colombara, D.; Islam, M. S. *Phys. Chem. Chem. Phys.* **2012**, *14*, 7229−33.
(12) Yan, C.; Su, Z.; Gu, E.; Cao, T.; Yang, J.; Liu, J.; Liu, F.; Lai, Y.; Li, J.; Liu, Y. *RSC Adv.* **2012**, *2*, 10481.
(13) Zhou, J.; Bian, G.-Q.; Zhu, Q.-Y.; Zhang, Y.; Li, C.-Y.; Dai, J. *J. Solid State Chem.* **2009**, *182*, 259−264.
(14) Razmara, M. F.; Henderson, C. N. B.; Pattrick, R. A. D.; Bell, A. M. T.; Charnock, J. M. *Mineralogical Magazine* **1997**, *61*, 79−88.
(15) Kyono, A.; Kimata, M. *Am. Mineral.* **2005**, *90*, 162−165.
(16) Rodriguez-Lazcano, Y.; Nair, M. T. S.; Nair, P. K. *J. Electrochem. Soc.* **2005**, *152*, G635−G638.
(17) An, C.; Liu, Q.; Tang, K.; Yang, Q.; Chen, X.; Liu, J.; Qian, Y. *J. Cryst. Growth* **2003**, *256*, 128−133.
(18) Kresse, G.; Hafner, J. *Phys. Rev. B* **1993**, *47*, 558.
(19) Kresse, G.; Hafner, J. *Phys.Rev. B* **1994**, *49*, 14251.
(20) Kresse, G.; Furthmuller, J. *Comput. Mater. Sci.* **1996**, *6*, 15.
(21) Kohn, W.; Sham, L. J. *Phys. Rev.* **1965**, *A140*, 1133.
(22) Perdew, J. P.; Burke, K.; Ernzerhof, M. *Phys. Rev. Lett.* **1996**, *77*, 3865.
(23) Heyd, J.; Scuseria, G. E.; Ernzerhof, M. *J. Chem. Phys.* **2003**, *118*, 8207.
(24) Hyed, J.; Scuseria, G. E.; Ernzerhof, M. *J. Chem. Phys.* **2006**, *124*, 219906.
(25) Blochl, P. E. *Phys. Rev. B* **1994**, *50*, 17953.
(26) Kresse, G.; Joubert, D. *Phys.Rev. B* **1999**, *59*, 1758.
(27) Mostofi, A. A.; Yates, J. R.; Lee, Y.-S.; Souza, I.; Vanderbilt, D.; Marzari, N. *Comput. Phys. Commun.* **2008**, *178*, 685.
(28) Ramasamy, K.; Zhang, X.; Bennett, R. D.; Gupta, A. *RSC Adv.* **2013**, *3*, 1186.
(29) Regulacio, M. D.; Ye, C.; Lim, S. H.; Bosman, M.; Ye, E.; Chen, S.; Xu, Q.-H.; Han, M.-Y. *Chemistry* **2012**, *18*, 3127−3131.
(30) Matte, H. S. S. R.; Gomathi, a; Manna, A. K.; Late, D. J.; Datta, R.; Pati, S. K.; Rao, C. N. R. *Angew. Chem., Int. Ed. Engl.* **2010**, *49*, 4059−4062.
(31) Smith, R. J.; King, P. J.; Lotya, M.; Wirtz, C.; Khan, U.; De, S.; O'Neill, A.; Duesberg, G. S.; Grunlan, J. C.; Moriarty, G.; Chen, J.; Wang, J.; Minett, A. I.; Nicolosi, V.; Coleman, J. N. *Adv. Mater.* **2011**, *23*, 3944−3948.

(32) Bensch, W.; Ophey, J.; Hain, H.; Gesswein, H.; Chen, D.; Mönig, R.; Gruber, P. A; Indris, S. *Phys. Chem. Chem. Phys.* **2012**, *14*, 7509−7516.
(33) Bodenez, V.; Dupont, L.; Laffont, L.; Armstrong, a. R.; Shaju, K. M.; Bruce, P. G.; Tarascon, J.-M. *J. Mater. Chem.* **2007**, *17*, 3238.
(34) Bodenez, V.; Dupont, L.; Morcrette, M.; Surcin, C.; Murphy, D. W.; Tarascon, J.-M. *Chem. Mater.* **2006**, *18*, 4278−4287.
(35) Ii, D. D. V.; In, S.; Schaak, R. E.; Al, V. E. T. *ACS Nano* **2011**, 8852−8860.
(36) Niederberger, M.; Cölfen, H. *Phys. Chem. Chem. Phys.* **2006**, *8*, 3271−3287.
(37) Zhou, L.; O'Brien, P. *J. Phys. Chem. Lett.* **2012**, *3*, 620−628.
(38) Coehoorn, R.; Haas, C.; de Groot, R. A. *Phys. Rev. B* **1987**, *35*, 6203−6206.
(39) Temple, D. J.; Kehoe, A. B.; Allen, J. P.; Watson, G. W.; Scanlon, D. O. *J. Phys. Chem. C* **2012**, *116*, 7334−7340.
(40) Adachi, S. In *Optical Properties of Crystalline and Amorphous Semiconductors: Materials and Fundamental Principles*, 1st ed.; Kluwer Academic Publishers: Boston, MA, 1999; pp 207−208 .
(41) Dufton, J. T. R.; Walsh, A.; Panchmatia, P. M.; Peter, L. M.; Colombara, D.; Islam, M. S. *Phys. Chem. Chem. Phys.* **2012**, *14*, 7229−7233.
(42) Tritsaris, G. A.; Malone, B. D.; Kaxiras, E. *J. Appl. Phys.* **2013**, *103*, 233507.